Measurements of Radiation Effects in DC-coupled Low Gain Avalanche Detectors

Honors Thesis

Seth Medina

University of New Mexico

April 2026

Advisors: Sally Seidel & Jiahe Si

Abstract

The effects of radiation damage on DC-coupled low gain avalanche detectors (LGADs) were studied. Measurements of leakage current, capacitance, and other characteristics, were taken of these detectors after exposure to 400 MeV protons of various fluences. These measurements were then compared to previous measurements of the same detectors before irradiation. These measurements will provide guidance for fast-timing instrumentation at future collider experiments.

Acknowledgments

I would like to thank my advisors Sally Seidel and Jiahe Si for their continual support throughout this project, as well as the rest of the UNM Collider Physics and Particle Instrumentation Group for their assistance with this project. I would also like to thank Gregor Kramberger and the Jožef Stefan Institute for providing the detectors used in this experiment.

Contents

1 INTRODUCTION **1**

1.1 Motivation for this Research . . . 1

1.2 The Large Hadron Collider & ATLAS Detector . . . 2

1.3 Semiconductors in Particle Physics . . . 3

1.4 Signal Formation . . . 6

1.5 Sensors . . . 7

1.5.1 LGAD Sensors . . . 7

1.5.2 PIN Diodes . . . 8

1.6 Radiation Damage . . . 8

2 EXPERIMENTAL PROCEDURE **9**

2.1 Environmental Setup . . . 9

2.1.1 Detector Configurations & Irradiation Process . . . 9

2.1.2 Probe Station Environment . . . 10

2.2 IV Measurement Setup . . . 10

2.3 CV Measurement Setup . . . 11

3 MEASUREMENTS **12**

3.1 Dosimetry . . . 12

3.2 LGADs . . . 13

3.3 PINs . . . 16

4 ANALYSIS OF UNCERTAINTIES **19**

4.1 CV Measurements . . . 19

4.1.1 Systematic Uncertainty . . . 19

4.1.2 Statistical Uncertainty . . . 19

4.2 IV Measurements . . . 21

4.2.1 Systematic Uncertainty . . . 21

4.2.2 Statistical Uncertainty . . . 21

5 CONCLUSIONS **22**

References **24**

Appendix **26**

1 INTRODUCTION

1.1 Motivation for this Research

The most successful theory in particle physics is the Standard Model, which describes the known particles in our universe and how they interact with each other. The Standard Model contains 6 quarks, 6 leptons, and their respective anti-particles, 4 gauge bosons, which govern the interactions among the quarks and leptons and explain 3 of the 4 fundamental forces, and the Higgs boson; these are shown in Fig. 1.

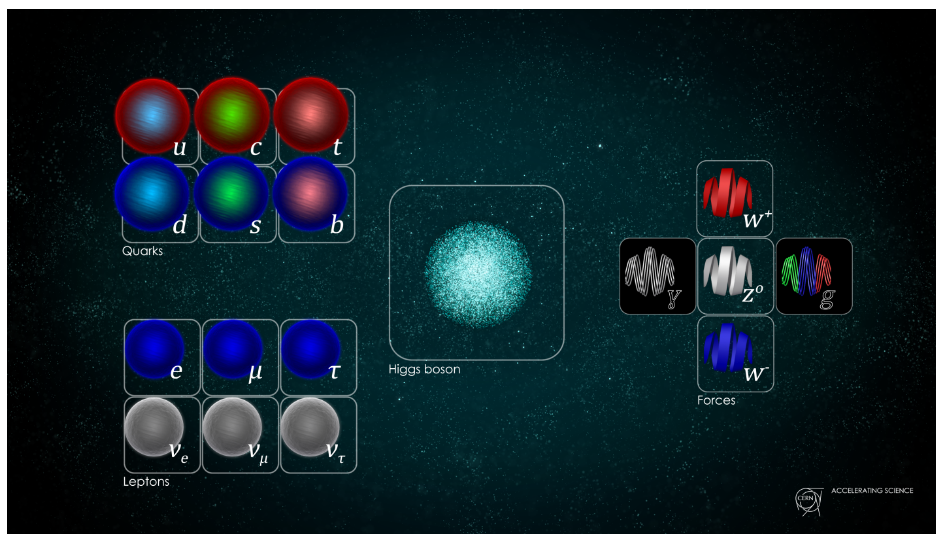

Figure 1: The particles included in the Standard Model of Particle Physics [1].

Despite the success of the Standard Model, there are still gaps in the current understanding of particle physics. These include missing explanations for dark matter, dark energy, neutrino mass, and matter domination. Explanations for these problems have prompted physicists to look for processes beyond the Standard Model, with new experiments. As these experiments become more precise and operate at increasing energy and luminosity, it is imperative that their detectors can resolve events in time and space, and continue to provide data under the continuous radiation damage incurred by high energy collider experiments.

1.2 The Large Hadron Collider & ATLAS Detector

The Large Hadron Collider (LHC) at CERN is the largest particle accelerator in the world with a 27 km circumference. It is situated as deep as 175 m underground on the Franco-Swiss border near Geneva, Switzerland. The tunnel houses a ring that accelerates hadrons, mostly protons, and sometimes heavy ions like lead, to speeds near the speed of light. Electric fields accelerate them to near light speed; and magnets guide them around the tunnel. Each beam is accelerated to an energy of 6.8 TeV, and they collide with an energy of 13.6 TeV in the center of mass. These collisions are measured at the four major detectors along the LHC, the ATLAS, CMS, LHCb, and ALICE detectors shown in Fig. 2.

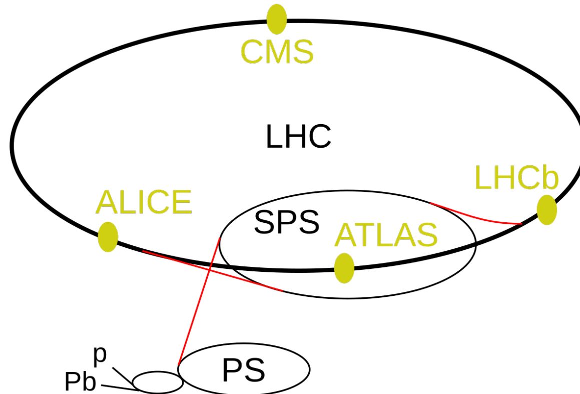

Figure 2: Diagram of the LHC and the 4 main detectors [2].

The ATLAS detector is the largest general purpose detector at the LHC and is designed to detect signals with the largest energy range of interest. The detector measures 25 m in diameter by 44 m in length. At the center of the detector is the interaction point of the beams where 600 million collisions per second occur [3]. These events are observed using the the many different sub-detectors within ATLAS shown in Fig. 3, with the Pixel detector as the closest sub-detector to the interaction point.

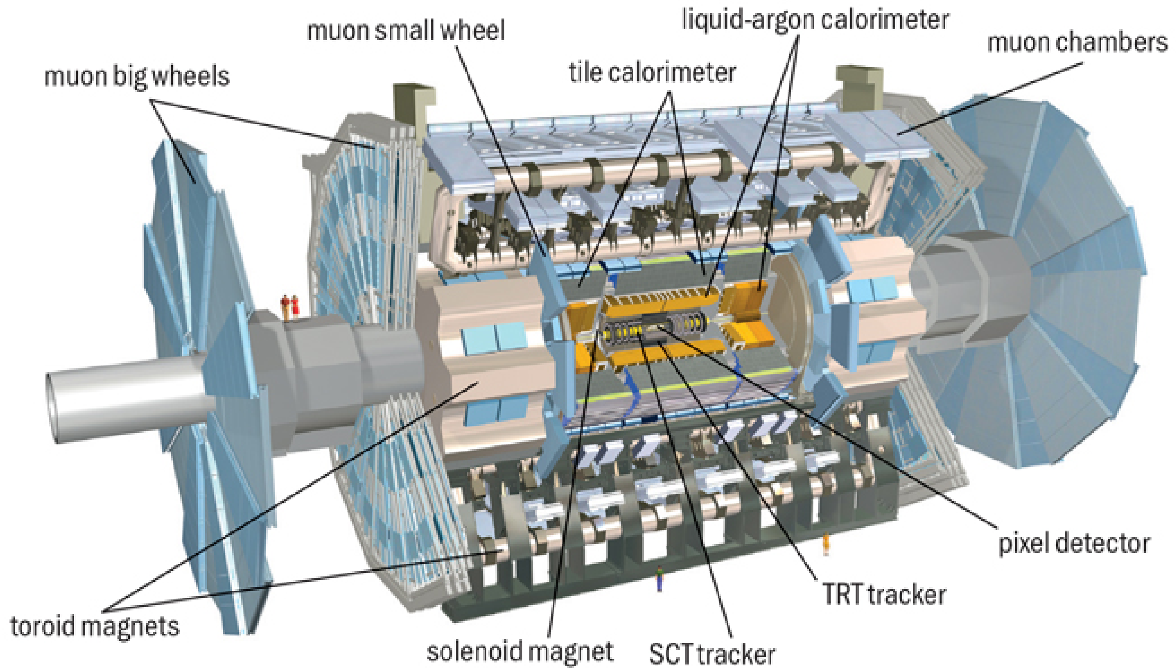

Figure 3: Image of the ATLAS detector [4].

The future of the LHC and ATLAS detector is the High Luminosity upgrade to the LHC (HL-LHC), which will increase the integrated luminosity by a factor of 10. Some of the planned upgrades to the HL-LHC are more powerful focusing magnets, reinforced radiation protection, and an upgraded accelerator chain for pre-acceleration [5]. The main detectors at the LHC, including ATLAS, are undergoing improvements to better accept the increased luminosity and withstand the increased radiation due to the higher number of particle interactions especially in the Pixel detector.

1.3 Semiconductors in Particle Physics

When a p-type and n-type semiconductor are brought into contact with one another, they form a pn junction. The difference in doping of the semiconductors creates a difference in their band structures. The Fermi level of the n-type material is closer to the conduction band, while the level of the p-type material is closer to the valence bend. This band gap causes the free electrons in the n-type semiconductor to diffuse into the p-type semiconductor. This creates an imbalance of charges, as the n-type material becomes positively charged due to the

deficit of electrons, and the p-type material becomes negatively charged after gaining those electrons. As a consequence, an electric field is created which opposes the further migration of charges. The electric field grows until it reaches equilibrium with the diffusion of electrons; this process is shown in Fig. 4.

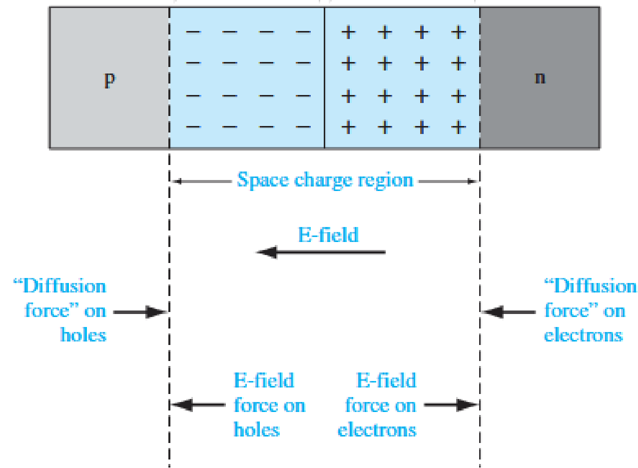

Figure 4: The space charge region, the electric field, and the forces acting on the charge carriers [6].

As the electrons travel from the n to the p region, the semiconductor is depleted of free charge carriers. The area with no free charge carriers is called the depletion region. The width of the depletion region can be changed by applying a potential difference across the pn junction.

To increase the width of the depletion region, a bias voltage with a higher potential on the n region and lower potential on the p region can be applied, creating what is called a reverse bias condition. The potential difference can be increased until the entire n-type region is fully depleted of charge carriers. At this point, the semiconductor behaves as an insulator as there are no free charge carriers to create a current. However; thermal excitation of electrons can still contribute to a small current called leakage current [7]. Fig. 5 shows how the pn junction is changed with open circuit and reverse bias voltages applied.

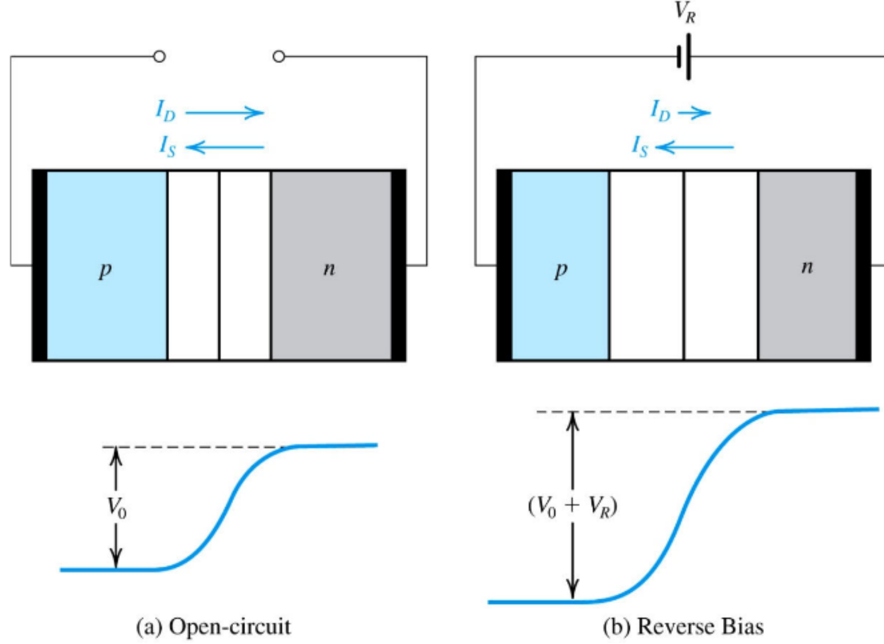

Figure 5: The pn junction in (a) equilibrium, (b) reverse bias [8].

Since the pn junction leads to a separation of positive and negative charges in the depletion region, the pn junction must have a related capacitance. Increasing the reverse bias voltage of the system will increase the size of the depletion region by removing thermally ionized pairs. This relation between capacitance and bias voltage is given by

$$C = \frac{dQ}{dV_R}, \tag{1}$$

where C is the capacitance of the depletion region, dQ is the differential charge, and dV_R is the increase in reverse bias voltage [6].

Semiconductor devices have been a key part of modern particle physics experiments for their excellent spatial resolution, and more recently their use as precise timing detectors. Those most often used are made of silicon. This silicon can have its properties changed by introducing substitutional impurities into the silicon lattice. By introducing a Group V atom such as phosphorus, four of the five valence electrons in the phosphorus will form covalent bonds with the four nearest neighboring silicon atoms. The extra valence electron is loosely bound to the phosphorus atom, meaning the electron is not confined to the range of a specific nucleus. Because of this weakly bound electron, a phosphorus atom is called a donor or n-type

dopant. If instead we introduce a Group III atom such as boron, its three valence electrons will form covalent bonds with three silicon atoms. The fourth silicon atom will not have a covalent bond, but will be able to accept an electron from neighboring atoms. Because of the incomplete silicon shell, a boron atom is called an acceptor atom and a semiconductor doped with boron is a p-type semiconductor. When a charged particle passes through a semiconductor detector, it interacts with the electrons in the silicon, causing them to either excite into a higher orbital, or ionize, creating electron-hole pairs. Once these electron-hole pairs are created, the electrons drift towards the n^{++} (highly n-type), and the holes drift towards the p^{++} (highly p-type) layers as is shown in Fig. 6 [7].

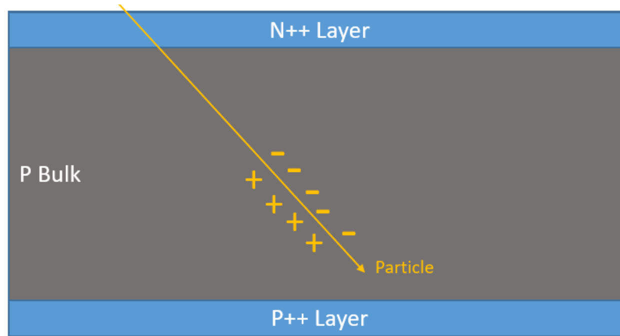

Figure 6: Diagram of a cross section of a silicon sensor creating e-h pairs due to an ionizing particle.

1.4 Signal Formation

When a charged particle crosses a silicon sensor and creates e-h pairs, those e-h pairs induce some charge on the electrodes. When a reverse bias voltage is applied, those charges drift towards the electrodes. The drift velocity $\mathbf{v}$ is given by

$$\mathbf{v} = \mu \mathbf{E}, \tag{2}$$

where μ is the mobility of a charge carrier under an electric field, and $\mathbf{E}$ is the electric field associated with the bias voltage. Electrons have a drift velocity of 1350 $\frac{cm^2}{V \cdot s}$, and holes have a drift velocity of 480 $\frac{cm^2}{V \cdot s}$ in silicon. The faster drift velocity of electrons in silicon makes them the preferred signal collecting charged particle [9].

This induced current can be calculated using the Shockley-Ramo Theorem which states,

$$i = q\mathbf{v} \cdot \mathbf{E_0}, \tag{3}$$

where i is the induced current, $\mathbf{v}$ is the drift velocity of charge q, and $\mathbf{E_0}$ is the weighting field which describes the coupling between the charge q and its electrode [10]. Once all of the charges have reached the electrode, the signal current creation is complete, and the signal can be full read out.

1.5 Sensors

1.5.1 LGAD Sensors

The basic structure of the LGAD remains the same as the semiconductor detectors discussed in Section 1.3 with a bulk layer between an n-type and a p-type electrode. What separates LGADs from other detectors is the presence of a highly doped p-type gain layer beneath the n-type electrode. This creates a large electric field. When the electric field is high enough, about 300 kV/cm for silicon, the electrons gain enough kinetic energy to ionize more silicon creating more e-h pairs which leads to an amplified signal; this difference between the PIN diode (see below) and the LGAD is shown in Fig. 7.

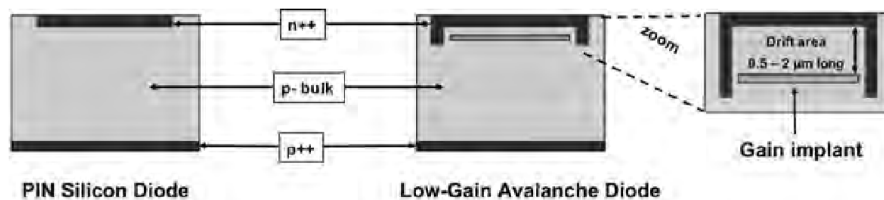

Figure 7: Diagram of a cross section of a PIN diode (left), and LGAD detector (right), characterized by the p-type gain implant [7].

Multiple LGAD designs have been developed, however these measurements choose to focus specifically on the DC-coupled LGAD. In addition to the diagram in Fig. 7, the measured LGADs have a guard ring to insulate the bulk from external currents and structure the internal electric field.

1.5.2 PIN Diodes

P-type Intrinsic N-type (PIN) diodes are a type of silicon detector that contains an intrinsic semiconductor region between an n-type and a p-type layer. This type of detector is a good representation of a semiconductor detector described in Section 1.3 of this paper. The simple structure of these diodes lacking a gain layer makes them the choice of semiconductor detector to compare the results of the LGADs excluding gain layer features, at different radiation doses [11].

1.6 Radiation Damage

When a particle crosses a silicon detector, it imparts some of its energy to the electrons and nuclei. The effects of the energy on the silicon detector can be classified into two categories: ionizing radiation which damages the surface, and non-ionizing radiation which damages the bulk.

Ionizing radiation damages bonds at the surface of the detector. The formation of the damage layer on the surface traps positive charges at the interface between the silicon and silicon dioxide layers. The trapped charges then induce a negative surface charge which can strongly influence the breakdown voltage and capacitance of a sensor [12].

Non-ionizing radiation causes displacements within the silicon lattice of the bulk of the sensor. The disrupted lattice develops bands in the "forbidden" region that provide a reduced potential for promotion from the valence to conductor band [13]. Nonionizing radiation can also displace the dopant atoms inside the lattice in a process called either acceptor or donor removal depending on the atom displaced. While not changing the doping of the silicon bulk, the displacement of the doping atoms causes a change in the effective doping of the bulk. This effective doping N_{eff} is directly proportional to the depletion voltage V_{dep} of the sensor given by

$$V_{\text{dep}} = \frac{q|N_{\text{eff}}|d^2}{2\epsilon\epsilon_0} \tag{4}$$

where d is the thickness of the device, q is the elementary charge, ϵ is the relative electric

permittivity of silicon, and ϵ_0 is the vacuum electric permittivity [14].

With the future HL-LHC upgrade, the integrated luminosity is expected to increase by a factor of 10, correlating to an anticipated increase in radiation levels by a factor of 10. This will increase the frequency of both types of radiation damage on the detector. This need to withstand the increased radiation of the future HL-LHC has led to the design of timing detectors with finer granularity in the sensor, reduced mass, and faster front ends [14].

2 EXPERIMENTAL PROCEDURE

2.1 Environmental Setup

2.1.1 Detector Configurations & Irradiation Process

The sensors are produced on wafers containing four detectors: one PIN diode and 3 LGADs. The active region across all the sensors is 50 μm thick. The major physical difference between the detectors is the plating on the electrode, where the wafers with the V1R5 label have a metal plated electrode, while the wafers with labels W1R2 and W4-12 have no plating on their electrodes. The wafers were placed on a board on different layers below aluminum foils. They were then irradiated using a 400 MeV proton beam to different fluences by collaborators at Los Alamos National Laboratory. The target fluences for the detectors were $2 \times 10^{14}\ \frac{n_{eq}}{cm^2}$, $4 \times 10^{14}\ \frac{n_{eq}}{cm^2}$, $8 \times 10^{14}\ \frac{n_{eq}}{cm^2}$, and $1.2 \times 10^{15}\ \frac{n_{eq}}{cm^2}$, where the unit n_{eq} is the equivalent fluence of a 1 MeV neutron. The radiation dose can be precisely measured by measuring the activation of the $5 \times 5 \times 1$ mm^3 aluminum foil that was mounted on the same board directly on top of each LGAD during the irradiation process. The irradiated detectors were then annealed by heating, and then stored below 0° C by collaborators in the UNM Collider Physics and Particle Instrumentation Group. Before measurements of the irradiated sensors were taken, the case containing them was taken out of the freezer and was allowed to rise above freezing in a bag filled with pure N_2 gas to prevent condensation from forming on the sensors when removed from their case.

2.1.2 Probe Station Environment

A probe station is used for both current and capacitance measurements. This probe station is in a clean room environment to minimize contamination, and is fully enclosed in a metal box to avoid any light interfering with the measurements; the probe station can be seen in Fig. 8. When measured, the wafer is placed on a Peltier thermal chuck which maintains the temperature of the unirradiated sensors at 20° C, and the irradiated detectors at −25° C. To avoid frost buildup on the irradiated detectors at low temperatures, N_2 air jets are placed over the wafer to prevent water vapor from condensing and freezing near the wafer.

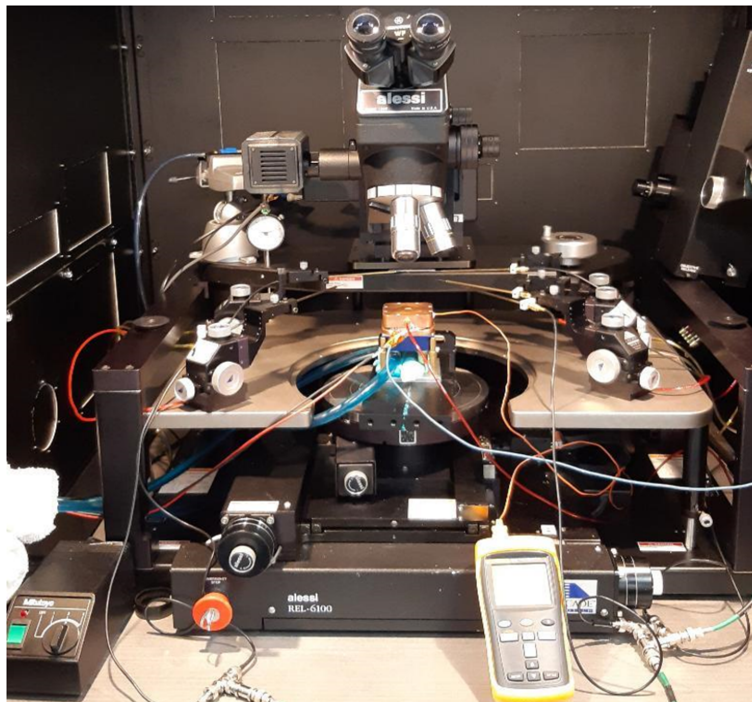

Figure 8: Photograph of the probe station inside the dark enclosure with the door open, taken at UNM.

2.2 IV Measurement Setup

When measuring the leakage current versus reverse bias voltage (IV) one probe is placed on the electrode connected to a picoammeter, and a second is placed on the guard ring and is grounded. A reverse bias voltage is applied using a Keithley 2410 Source Measure Unit. The leakage current of the whole detector is measured using the Keithley 6487 picoammeter and recorded as a function of reverse bias voltage on the data collecting computer; a diagram of

this setup is shown in Fig. 9.

The IV curve of the detector is measured over the range of 0 to 600 V, where 600 V is chosen to be the maximum voltage sustainable by the 50 μm thick active region of the detectors. However, the measurement will be terminated at a lower bias if the measured leakage current exceeds the set compliance current, on the order of 10^{-6} A. This sharp increase in leakage current past the compliance current shows the breakdown voltage of the sensor, showing what voltages the detectors must be operated under.

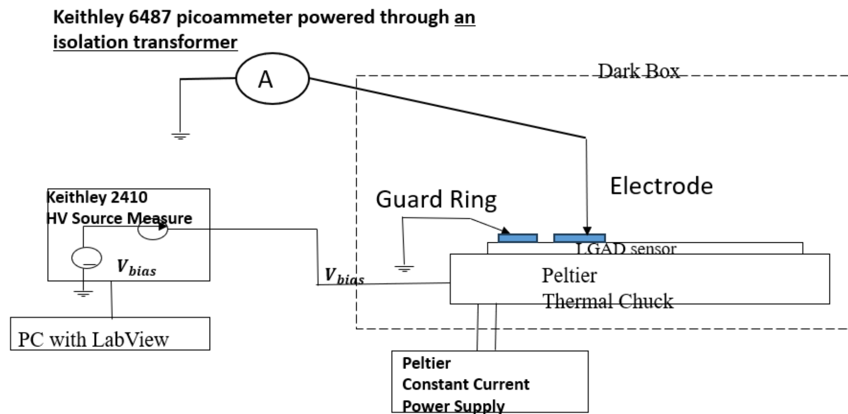

Figure 9: Diagram showing the setup for IV measurements.

2.3 CV Measurement Setup

To measure the capacitance with respect to voltage (CV) of the detectors, the first probe is placed on the electrode connected to the low end of an isolation box, and a second is placed on the guard ring and is grounded. A reverse bias voltage is applied to the isolation box using the Keithley 237 Source Meter. The isolation box separates the AC and DC voltages collected from the detectors so that the LCR meter can measure the capacitance at several frequencies {1 kHz, 3 kHz, 10 kHz, 100 kHz, and 1 MHz}; a diagram of this setup is shown in Fig. 10. Before a CV measurement is taken, an open correction is taken with the probes raised to measure the system capacitance which is accounted for in the eventual measurement. After the open measurement, the probes are lowered and CV data is recorded onto the computer for all frequencies.

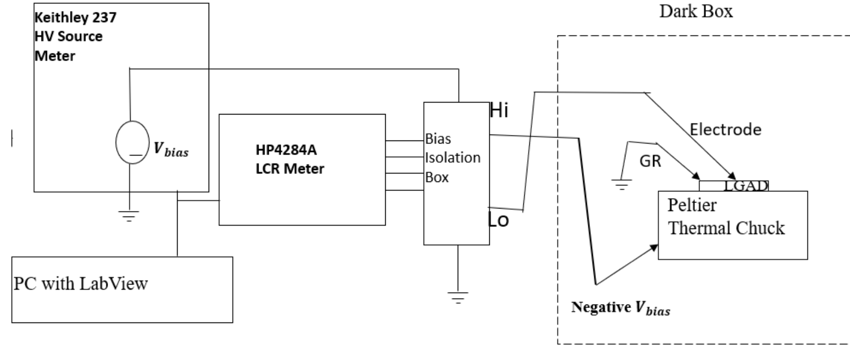

Figure 10: Diagram showing the setup for CV measurements.

The CV measurement is taken over the range of voltages 0 to 60 V, because the detectors are fully depleted of charge at or below 60 V.

3 MEASUREMENTS

3.1 Dosimetry

After the sensors are irradiated, the aluminum foil that was placed on top of the wafers can be measured. The process involves using a gamma spectrometer to measure the gamma radiation coming from the foil. This gamma radiation is produced by sodium-22 isotopes which are created in the aluminum during the irradiation process. After this measurement was taken by collaborators in by collaborators in the UNM Collider Physics and Particle Instrumentation Group, the data was received for the radiation of the foils and I used the data to determine the fluence of each sensor, based on its position relative to the foils during irradiation. The comparison between these measured fluences and the target fluences for these sensors can be seen in Table 1 in the Appendix.

The measured fluences of the detectors are the same for the PIN and LGAD 1 and are the same for LGADs 2 and 3 on the same wafer; this is due to the measured aluminum foils' covering 2 sensors during irradiation. The repeated measured values between sensors on different wafers reflects the fact that the irradiation took place on the same board with the sensors in the same position relative to the foils, but further back on the board during irradiation. There is a lower uncertainty on the detectors on the W1R2-20, because the wafer

was placed between multiple foils allowing for a more accurate analysis.

3.2 LGADs

The initial leakage current increases when the sensors are irradiated. The observed breakdown voltage occurs at higher voltages as the fluence increases. There are no qualitative differences between the plated and unplated sensors with no radiation, however the breakdown voltages of the unplated sensors are larger than those of the LGADs with plated electrodes at the same fluence. These features can be seen in Fig. 11.

The observed difference between the plated and unplated LGADs is the larger initial capacitance and lower gain layer depletion voltage of the unirradiated LGAD with no plating (W1R2-11) when compared to its plated counterpart (V1R5-36). The CV curves of the irradiated LGADs show an increase in capacitance at 25 V which is not fully understood. A similar increase in capacitance was observed in the measurements in a different study [15]. Those authors speculate, "The sudden increase of free charge carriers from multiplication can lead to a smaller depleted region around the junction, effectively increasing the measured capacitance." The presentation of the data in Fig. 12 as capacitance versus voltage rather than the standard inverse square of the capacitance versus voltage were chosen to highlight this behavior.

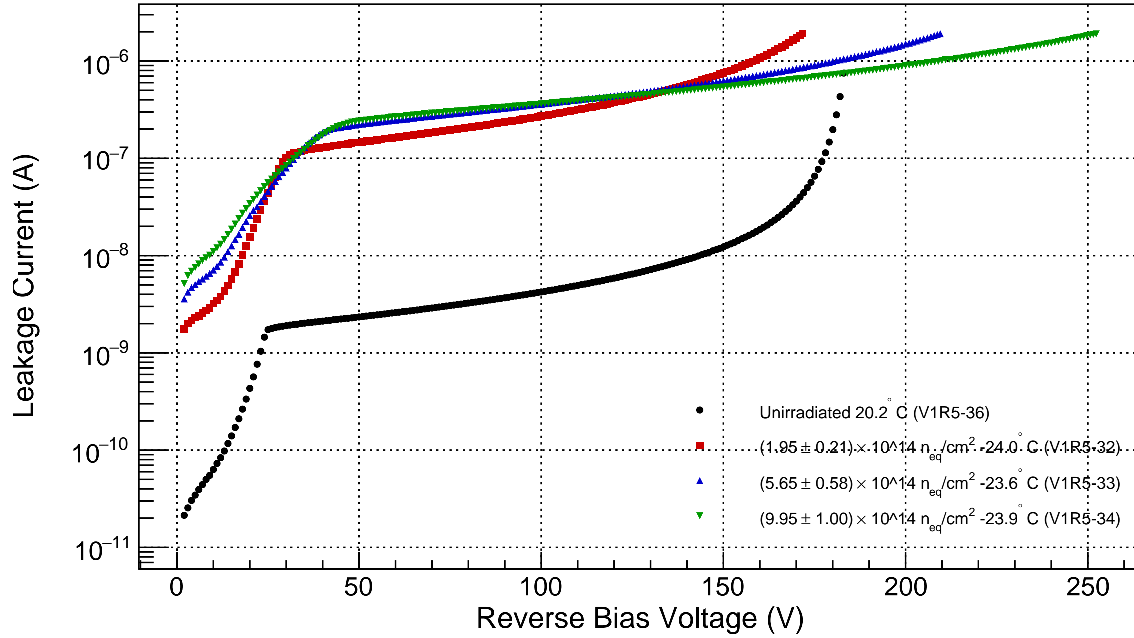

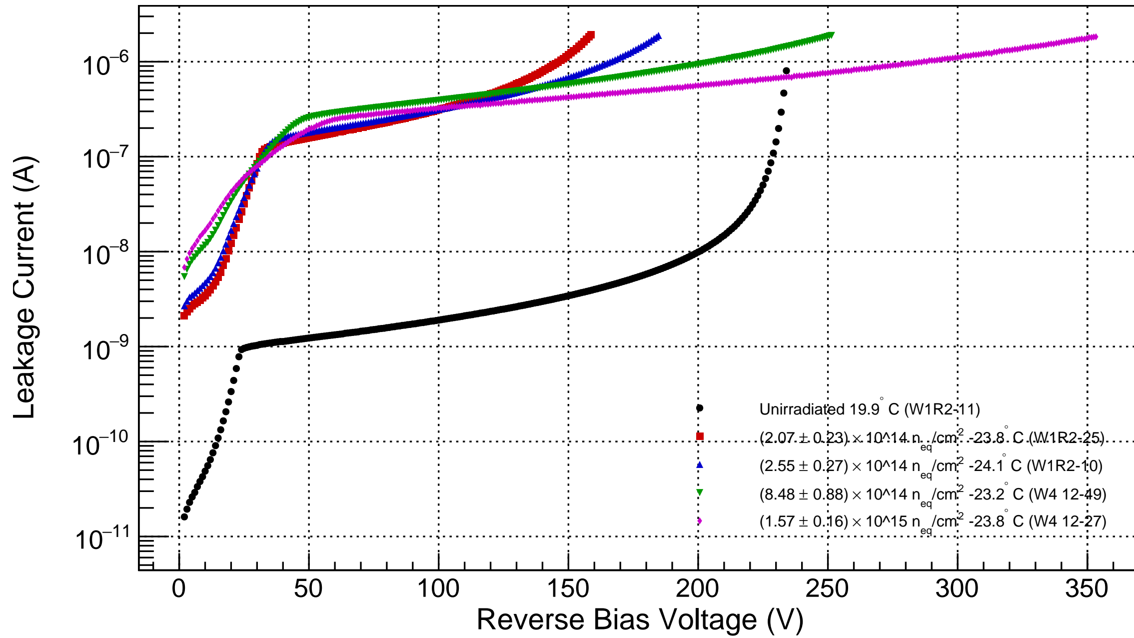

Figure 11: Leakage current versus reverse bias voltage of LGADs, with errors not large enough to plot, with plated electrodes (top) and unplated electrodes (bottom). These plots are representative of all measured sensors. The applied proton fluences are shown in the legend.

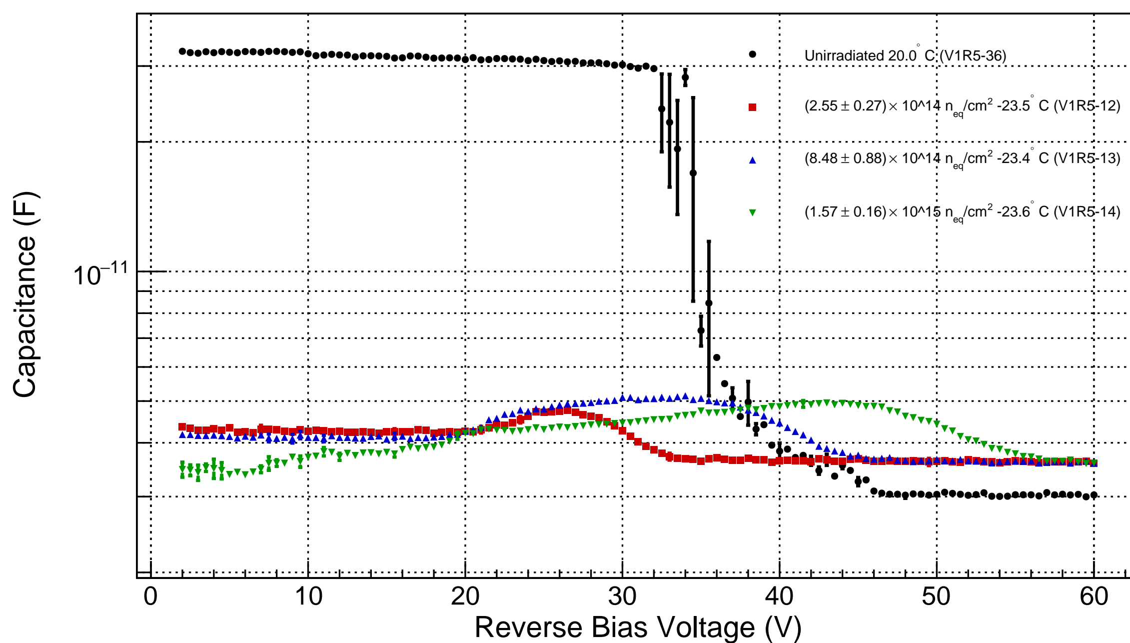

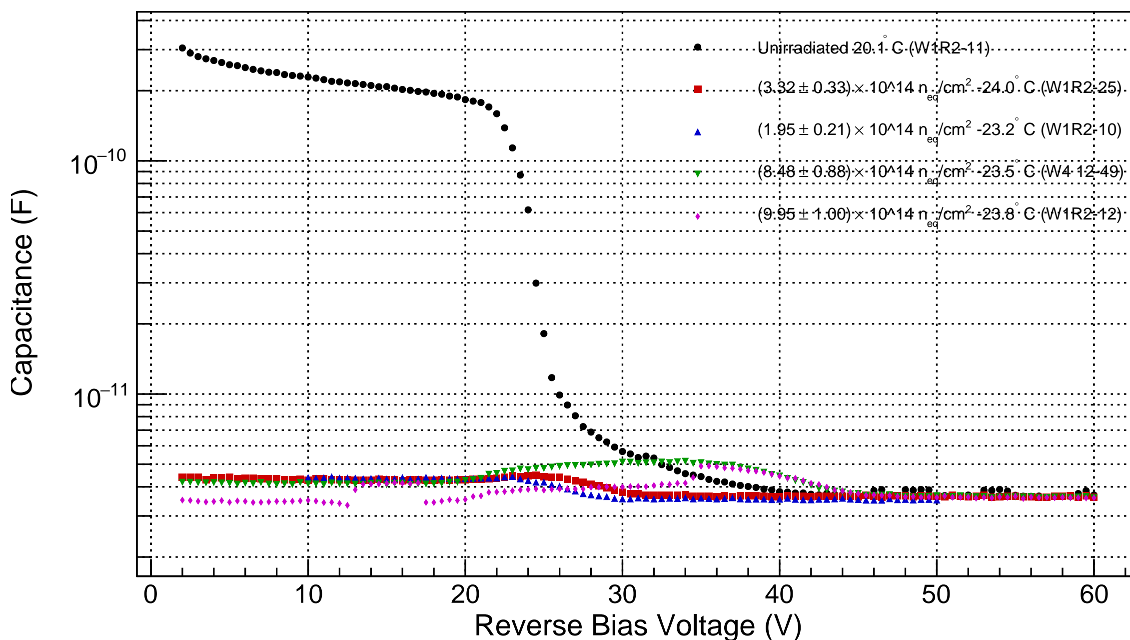

Figure 12: Capacitance versus reverse bias voltage of LGADs at 10 kHz with plated electrodes (top) and unplated electrodes (bottom). These plots are representative of all measured sensors. The applied proton fluences are shown in the legend.

3.3 PINs

The IV curves for the PIN diodes, shown in Fig. 13, show an increase in leakage current as the fluence increases. The leakage current of the detectors shown never reached the compliance current of 10^{-6} A, showing no breakdown. There is a notable increase in leakage current in the unplated, unirradiated sensor (W1R2-11) at high voltages, however the current does not exceed 10^{-9} A, so the sensor still shows no breakdown.

The CV curves for the PIN diodes, shown in Fig. 14, show simpler behavior than those of the LGADs, with immediate depletion in the case of all but the unirradiated plated sensor (V1R5-36). Both of the unirradiated sensors show an initial capacitance falling until the sensor is fully depleted, while all of the irradiated detectors begin fully depleted. This effect, which is unexpected, is still under study.

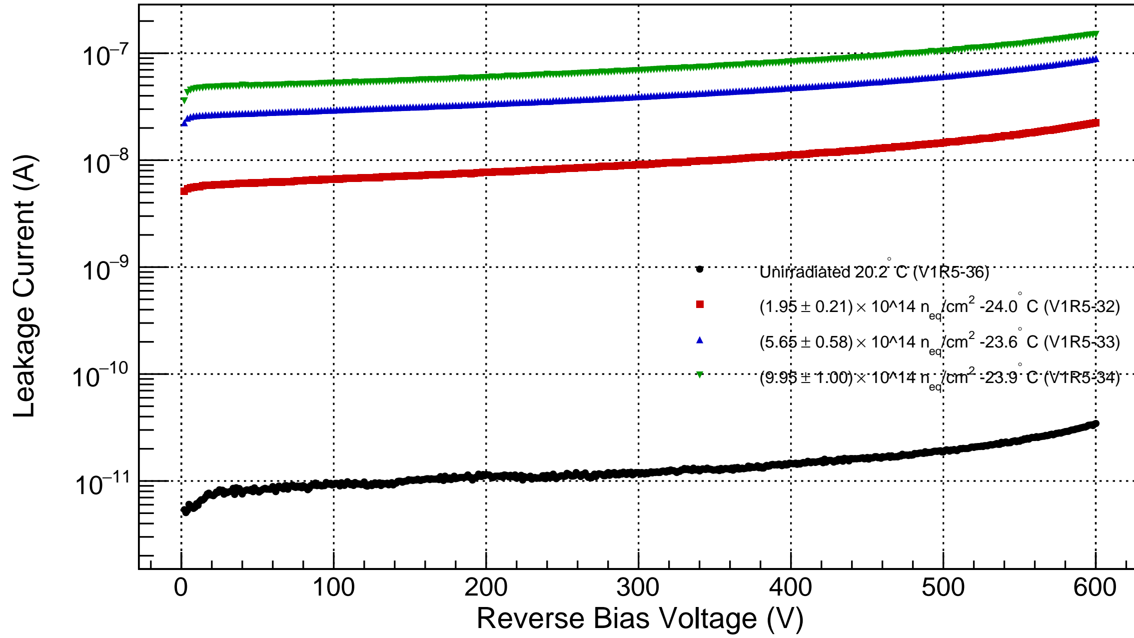

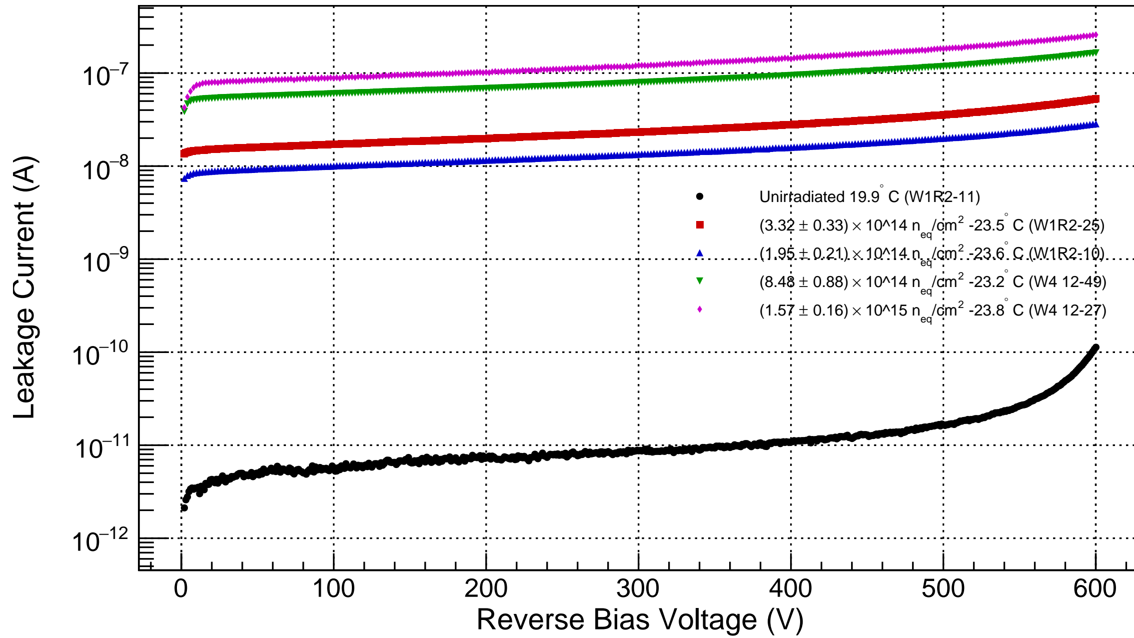

Figure 13: Leakage current versus reverse bias voltage of PIN diodes, with errors not large enough to plot, with plated electrodes (top) and unplated electrodes (bottom). These plots are representative of all measured sensors. The applied proton fluences are shown in the legend.

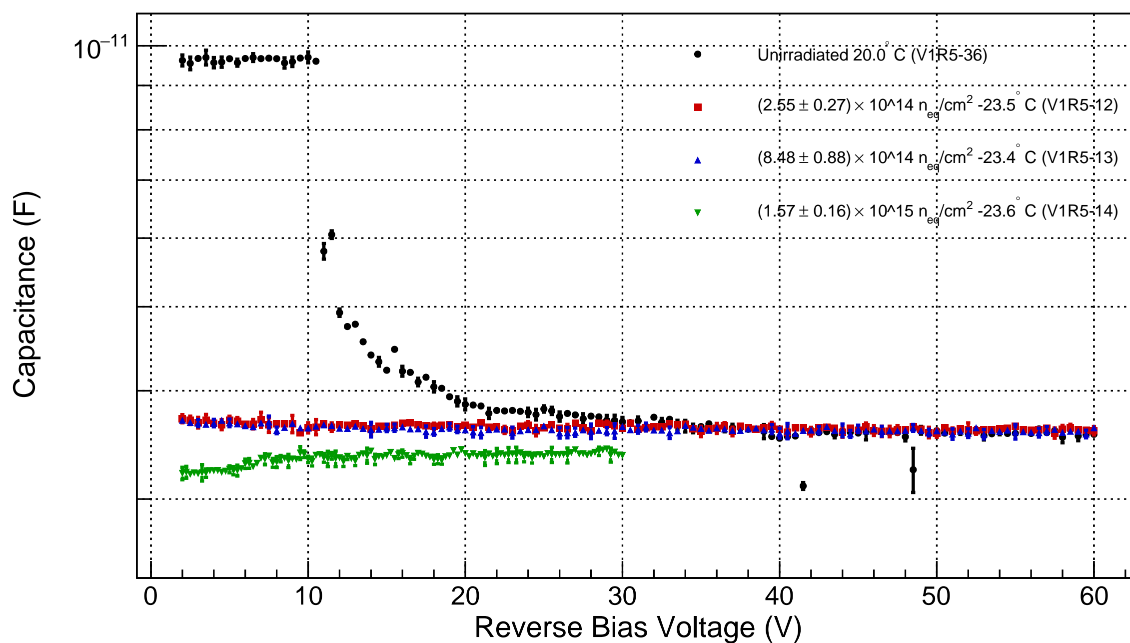

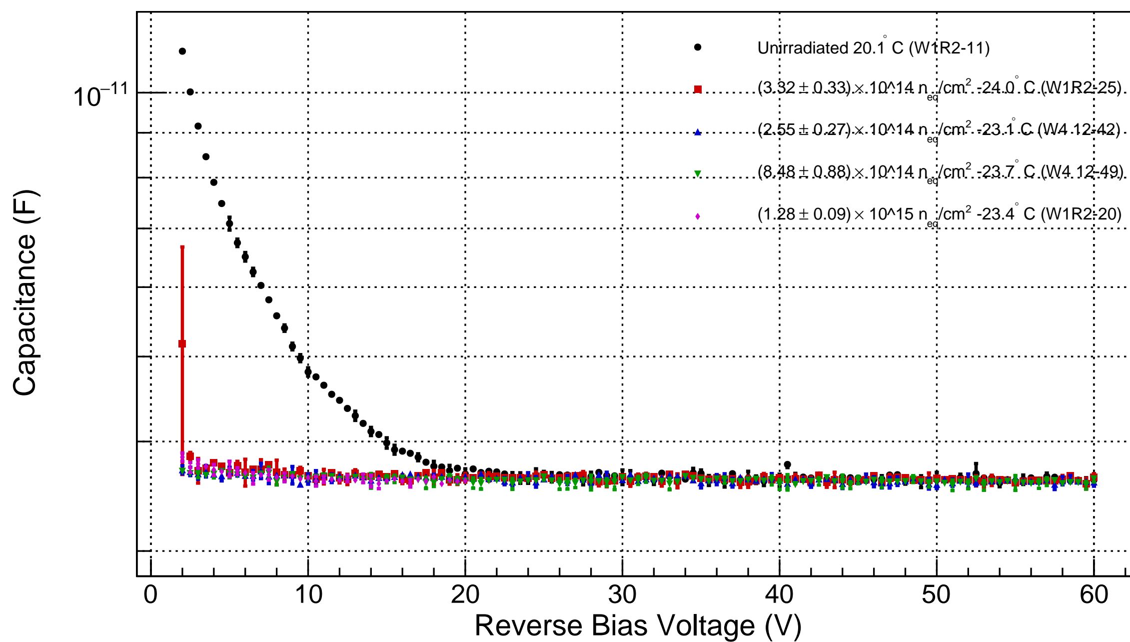

Figure 14: Capacitance versus reverse bias voltage of PIN diodes at 10 kHz with plated electrodes (left) and unplated electrodes (right). These plots are representative of all measured sensors. The applied proton fluences are shown in the legend.

4 ANALYSIS OF UNCERTAINTIES

4.1 CV Measurements

4.1.1 Systematic Uncertainty

To estimate the gain layer and full depletion voltages of the LGADs, the systematic uncertainty of the experimental setup, typically 1.9%, needs to be characterized. The error introduced by the equipment is as follows: (±0.3% + 100) fA for the Keithley 237 Source Meter, ±0.34% for the HP4284A LCR Meter, and a ±0.5°C uncertainty in temperature which leads to a ±1.82% uncertainty [16].

4.1.2 Statistical Uncertainty

To measure the depletion voltages of the sensors, the CV curves are measured as $\frac{1}{C^2}$ versus voltage. This emphasizes the effect of the dopant concentration, which influences the slope of the curve given by the equation,

$$\frac{1}{C^2} = \frac{2(V_{bi} + V_R)}{e\epsilon_s N_d} \tag{5}$$

Here C is the measured capacitance, V_{bi} is the constant potential barrier, V_R is the applied reverse bias voltage, ϵ_s is the electric permittivity, and N_d is the dopant concentration [6]. Three lines are fitted to the $\frac{1}{C^2}$ curve, representing three regions of different dopant concentrations in the sensor, the p+ gain layer, the silicon bulk, and the p++ electrode in order of voltage. Their intersections show the gain layer and bulk layer depletion points. When in use, the sensor must be operated at a voltage higher than the full depletion, because the sensor is depleted of free charges,. The lines are fitted using TGraph in the ROOT analysis package at chosen intervals along the curve including uncertainty measured by the HP4284A LCR meter. The intersection points are calculated from the fitted lines using the equation,

$$V = \frac{b_2 - b_1}{m_1 - m_2}, \tag{6}$$

where b_1 and m_1 are the intercept and slope of the leftmost fitted line, and b_2 and m_2 are the intercept and slope of the rightmost fitted line. Propagation of uncertainty is used to determine the statistical uncertain of the voltages from the uncertainties of the slopes and intercepts of the fitted lines. The statistical uncertainty is combined with the systemic uncertainty to compute the total uncertainty of the gain layer and full depletion voltages. An example of the fitting and the errors is shown in Fig. 15, and the depletion voltages for all unirradiated sensors is shown in Table 2 in the Appendix. The depletion voltages of the irradiated sensors could not be determined using this method due to the feature of capacitance increase shown in Fig. 12.

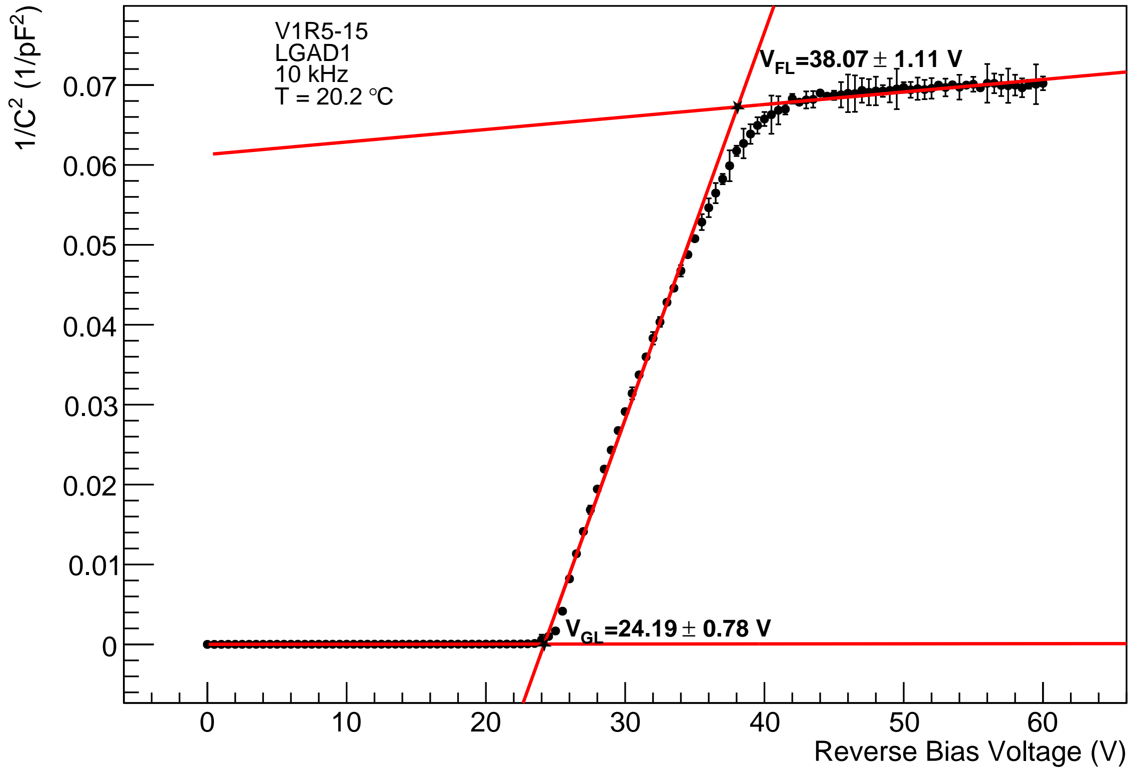

Figure 15: Example of a $\frac{1}{C^2}$ versus voltage plot of an LGAD at 10 kHz fitted with lines to estimate the gain layer and full layer depletion voltages with errors.

4.2 IV Measurements

4.2.1 Systematic Uncertainty

Before the IV curves are used to determine the breakdown voltages of the LGADs, the systematic uncertainty of the experimental setup, typically 1.9%, needs to be characterized. The error introduced by the equipment is as follows: (±0.3% + 100) fA for the Keithley 237 Source Meter, (±0.1% + 1) µA and a ±0.5°C uncertainty in temperature which leads to a ±1.82% uncertainty [16].

4.2.2 Statistical Uncertainty

The direct relationship between leakage current and bias voltage ideally ends after full depletion, however, when the sensor begins to breakdown the leakage current is multiplied by a factor given by the equation,

$$M = \frac{1}{1 - (V_R/V_{BD})^m}, \tag{7}$$

Here V_{BD} is the breakdown, V_R is the applied reverse bias voltage, and m is a constant in the range of 3 to 6 [6]. Because this relation is based on unknown physical characteristics, different fit parameters are chosen. Two lines are fitted to the IV curve, one after the full depletion voltage, and another in the range of the compliance current, $V(I = 2\,\mu A) \pm 1.9\%$, this will ensure the breakdown voltage is before the sharp increase in leakage current that occurs before compliance. Their intersection shows the breakdown voltage estimate of the maximum voltage at which the LGADs can be operated. The lines are fitted using TGraph in the ROOT analysis package at chosen intervals along the curve including uncertainty measured by the Keithley 6487 picoammeter. The intersection points are calculated from the fitted lines using the equation,

$$V = \frac{b_2 - b_1}{m_1 - m_2}, \tag{8}$$

where b_1 and m_1 are the intercept and slope of the leftmost fitted line, and b_2 and m_2 are the intercept and slope of the rightmost fitted line. Propagation of uncertainty is used to determine the statistical uncertain of the voltages from the uncertainties of the slopes and intercepts of the fitted lines. The statistical uncertainty is combined with the systemic uncertainty to compute the total uncertainty of breakdown voltage. An example of the fitting and the errors is shown in Fig. 16, and the breakdown voltages for all measured LGADs is shown in Table 3 in the Appendix.

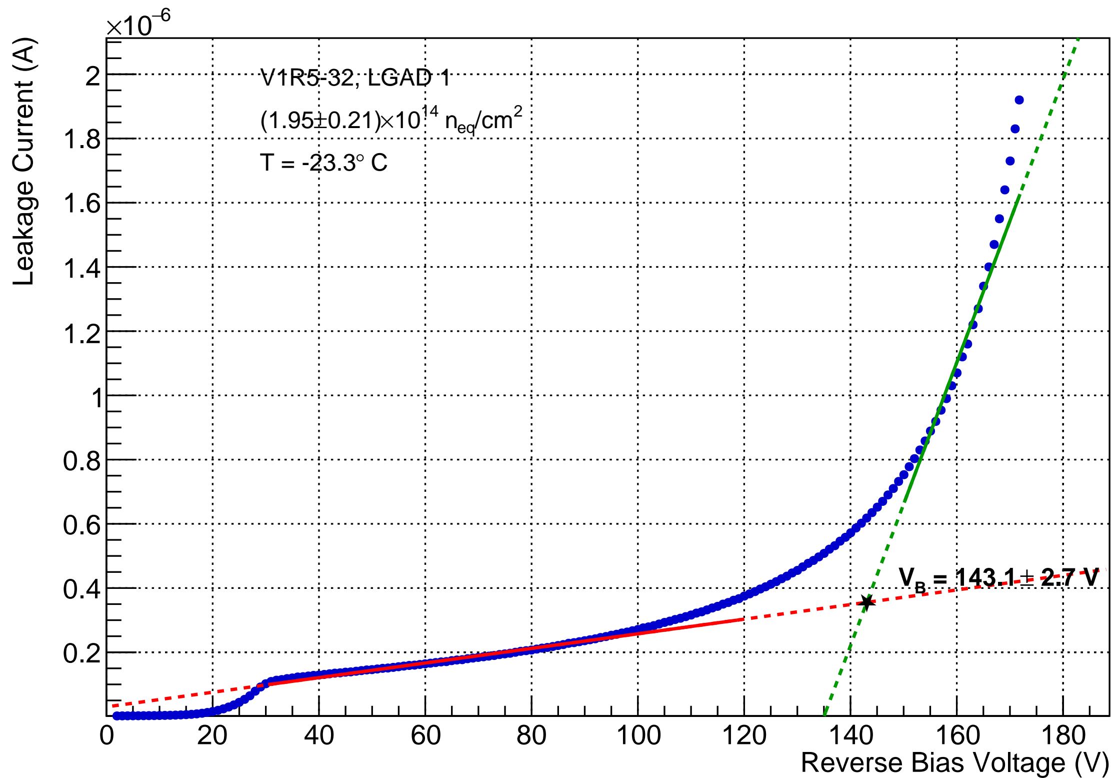

Figure 16: Example of a leakage current versus voltage plot of an LGAD, with errors not large enough to plot, fitted with lines to estimate the breakdown voltage with errors.

5 CONCLUSIONS

Electrical qualities of DC-LGADs as a function of radiation dose have been characterized. The measured fluence of the irradiated sensors was used to study the effect that the received dose had on the electrical qualities of the sensors with fluences up to 1.57×10^{15} $n_{\mathrm{eq}}/\mathrm{cm}^2$.

These qualities were measured by taking IV and CV measurements of the sensors. The radiation dose had the effect of increasing the leakage current, as well as increasing the breakdown voltage. The radiation also had the effect of increasing the capacitance of the sensors at higher voltages. This unexpected result in capacitance requires more research into its physical cause before complete operational voltage ranges can be determined. These measurements are important in determining the behaviors and operational voltage ranges of LGADs in the high fluence environments of future collider experiments such as the HL-LHC.

References

[1] CERN. The Standard Model of Particle Physics, 2024. URL https://home.cern/science/physics/standard-model.

[2] Horvath, Arpad. Diagram of the Large Hadron Collider (LHC). https://commons.wikimedia.org/wiki/File:LHC.svg, 2006.

[3] Aad, G., et al. The ATLAS experiment at the CERN Large Hadron Collider. *Journal of Instrumentation*, 3(08):S08003, 2008.

[4] Pequenao, Joao. Computer generated image of the whole ATLAS detector. 2008. URL https://cds.cern.ch/record/1095924.

[5] Apollinari, Giorgio and Brüning, O. and Nakamoto, Tatsushi and Rossi, Lucio. High Luminosity Large Hadron Collider HL-LHC. *arXiv:1705.08830*, 2017.

[6] Neamen, Donald A. and Biswas, Dhrubes. *Semiconductor physics and devices*. McGraw-Hill Higher Education, New York, 2011.

[7] Ferrero, Marco and Arcidiacono, Roberta and Mandurrino, Marco and Sola, Valentina and Cartiglia, Nicolò. *An Introduction to Ultra-Fast Silicon Detectors*. CRC press, 2021.

[8] Sedra, A. and Smith, K.C. *Microelectronic Circuits, 8th Edition*. Oxford University Press, Oxford, 2020.

[9] Anna, Peisert. Silicon microstrip detectors. In *Instrumentation in High Energy Physics*, pages 1–79. World Scientific, 1992.

[10] He, Zhong. Review of the Shockley–Ramo theorem and its application in semiconductor gamma-ray detectors. *Nucl. Instrum. and Meth. A*, 463(1-2):250–267, 2001.

[11] Laštovička-Medin, Gordana et al. Femtosecond laser studies of the single event effects in low gain avalanche detectors and PINs at ELI beamlines. *Nucl. Instrum. and Meth. A*, 1041:167321, 2022.

[12] Moscatelli, Francesco, et al. Combined bulk and surface radiation damage effects at very high fluences in silicon detectors: measurements and TCAD simulations. *IEEE Transactions on Nuclear Science*, 63(5):2716–2723, 2016.

[13] Lindström, Gunnar. Radiation damage in silicon detectors. *Nucl. Instrum. and Meth. A*, 512(1-2):30–43, 2003.

[14] Moll, Michael. Displacement damage in silicon detectors for high energy physics. *IEEE Transactions on Nuclear Science*, 65(8):1561–1582, 2018.

[15] Wiehe, Moritzet, et al. Study of the radiation-induced damage mechanism in proton irradiated low gain avalanche detectors and its thermal annealing dependence. *Nucl. Instrum. and Meth. A*, 986:164814, 2021.

[16] Hoeferkamp, M., et al. Characterization of Low Gain Avalanche Detector Prototypes' Response to Gamma Radiation. *Frontiers in Physics*, 10:838463, 2022.

Appendix

Dosimetric Values

Table 1: Comparison between the target fluence and measured fluence of all measured irradiated sensors.

Sensor	Target Fluence $\times 10^{14}$ ($n_{\text{eq}}/\text{cm}^2$)	Measured Fluence $\times 10^{14}$ ($n_{\text{eq}}/\text{cm}^2$)
W1R2-25 PIN	2	3.32 ± 0.33
W1R2-25 LGAD 1	2	3.32 ± 0.33
W1R2-25 LGAD 2	2	2.04 ± 0.22
W1R2-25 LGAD 3	2	2.04 ± 0.22
W4 12-43 PIN	2	2.07 ± 0.23
W4 12-43 LGAD 1	2	2.07 ± 0.23
W4 12-43 LGAD 2	2	1.32 ± 0.15
W4 12-43 LGAD 3	2	1.32 ± 0.15
V1R5-12 PIN	4	2.55 ± 0.27
V1R5-12 LGAD 1	4	2.55 ± 0.27
V1R5-12 LGAD 2	4	4.62 ± 0.48
V1R5-12 LGAD 3	4	4.62 ± 0.48
W1R2-10 PIN	4	1.95 ± 0.21
W1R2-10 LGAD 1	4	1.95 ± 0.21
W1R2-10 LGAD 2	4	3.47 ± 0.36
W1R2-10 LGAD 3	4	3.47 ± 0.36
W4 12-42 PIN	4	2.55 ± 0.27
W4 12-42 LGAD 1	4	2.55 ± 0.27
W4 12-42 LGAD 2	4	4.62 ± 0.48
W4 12-42 LGAD 3	4	4.62 ± 0.48
V1R5-32 PIN	4	1.95 ± 0.21
V1R5-32 LGAD 1	4	1.95 ± 0.21

Sensor	Target Fluence $\times 10^{14}$ ($n_{\mathrm{eq}}/\mathrm{cm}^2$)	Measured Fluence $\times 10^{14}$ ($n_{\mathrm{eq}}/\mathrm{cm}^2$)
V1R5-32 LGAD 2	4	3.47 ± 0.36
V1R5-32 LGAD 3	4	3.47 ± 0.36
V1R5-13 PIN	8	8.48 ± 0.88
V1R5-13 LGAD 1	8	8.48 ± 0.88
V1R5-13 LGAD 2	8	5.00 ± 0.51
V1R5-13 LGAD 3	8	5.00 ± 0.51
W1R2-27 PIN	8	5.65 ± 0.56
W1R2-27 LGAD 1	8	5.65 ± 0.56
W1R2-27 LGAD 2	8	3.16 ± 0.33
W1R2-27 LGAD 3	8	3.16 ± 0.33
W4 12-49 PIN	8	8.48 ± 0.88
W4 12-49 LGAD 1	8	8.48 ± 0.88
W4 12-49 LGAD 2	8	5.00 ± 0.51
W4 12-49 LGAD 3	8	5.00 ± 0.51
V1R5-33 PIN	8	5.65 ± 0.56
V1R5-33 LGAD 1	8	5.65 ± 0.56
V1R5-33 LGAD 2	8	3.16 ± 0.33
V1R5-33 LGAD 3	8	3.16 ± 0.33
V1R5-14 PIN	12	15.7 ± 1.6
V1R5-14 LGAD 1	12	15.7 ± 1.6
V1R5-14 LGAD 2	12	8.98 ± 0.92
V1R5-14 LGAD 3	12	8.98 ± 0.92
W1R2-20 PIN	12	12.8 ± 0.9
W1R2-20 LGAD 1	12	12.8 ± 0.9
W1R2-20 LGAD 2	12	7.59 ± 0.60
W1R2-20 LGAD 3	12	7.59 ± 0.60
W1R2-12 PIN	12	3.16 ± 0.33
W1R2-12 LGAD 1	12	9.95 ± 1.00

Sensor	Target Fluence $\times 10^{14}$ ($n_{\mathrm{eq}}/\mathrm{cm}^2$)	Measured Fluence $\times 10^{14}$ ($n_{\mathrm{eq}}/\mathrm{cm}^2$)
W1R2-12 LGAD 2	12	6.00 ± 0.61
W1R2-12 LGAD 3	12	6.00 ± 0.61
W4 12-27 PIN	12	15.7 ± 1.6
W4 12-27 LGAD 1	12	15.7 ± 1.6
W4 12-27 LGAD 2	12	8.98 ± 0.92
W4 12-27 LGAD 3	12	8.98 ± 0.92
V1R5-34 PIN	12	9.95 ± 1.00
V1R5-34 LGAD 1	12	9.95 ± 1.00
V1R5-34 LGAD 2	12	6.00 ± 0.61
V1R5-34 LGAD 3	12	6.00 ± 0.61

Depletion Voltages

Table 2: Measurements of gain layer and full depletion voltages with uncertainty of all measured unirradiated LGADs.

Sensor	Gain Layer Depletion (V)	Full Depletion (V)
V1R5-15 LGAD 1	24.19 ± 0.78	38.07 ± 1.11
V1R5-15 LGAD 2	23.94 ± 0.94	37.68 ± 1.31
V1R5-15 LGAD 3	23.92 ± 0.89	37.73 ± 1.31
V1R5-36 LGAD 1	31.84 ± 1.28	45.04 ± 1.77
V1R5-36 LGAD 2	29.46 ± 1.24	42.11 ± 1.39
V1R5-36 LGAD 3	23.97 ± 0.97	37.74 ± 1.41
W1R2-11 LGAD 1	23.79 ± 0.79	40.65 ± 1.45
W1R2-11 LGAD 2	29.69 ± 1.17	42.89 ± 1.72
W1R2-11 LGAD 3	23.07 ± 0.72	39.19 ± 1.28
W4 12-28 LGAD 1	26.32 ± 0.76	29.51 ± 0.83
W4 12-28 LGAD 2	26.35 ± 0.78	29.55 ± 0.83
W4 12-28 LGAD 3	26.34 ± 0.76	29.54 ± 0.83

Breakdown Voltages

Table 3: Measurements of breakdown voltages with uncertainty of all measured LGADs.

Sensor	Breakdown Voltage (V)
V1R5-15 LGAD 1	182.3 ± 3.5
V1R5-15 LGAD 2	182.6 ± 3.4
V1R5-15 LGAD 3	181.9 ± 3.5
V1R5-36 LGAD 1	167.5 ± 3.2
V1R5-36 LGAD 2	170.1 ± 3.3
V1R5-36 LGAD 3	170.6 ± 3.2
W1R2-11 LGAD 1	218.3 ± 4.1
W1R2-11 LGAD 2	217.3 ± 4.1
W1R2-11 LGAD 3	218.5 ± 4.2
W4 12-28 LGAD 1	172.3 ± 3.3
W4 12-28 LGAD 2	170.2 ± 3.4
W4 12-28 LGAD 3	172.0 ± 3.3
W1R2-25 LGAD 1	165.6 ± 3.2
W1R2-25 LGAD 2	167.7 ± 3.2
W1R2-25 LGAD 3	168.1 ± 3.1
W4 12-43 LGAD 1	139.3 ± 2.7
W4 12-43 LGAD 2	137.4 ± 2.6
W4 12-43 LGAD 3	137.0 ± 2.6
V1R5-12 LGAD 1	151.8 ± 2.9
V1R5-12 LGAD 2	155.2 ± 2.9
V1R5-12 LGAD 3	157.1 ± 3.0
W1R2-10 LGAD 1	175.5 ± 3.3
W1R2-10 LGAD 2	167.9 ± 3.2
W1R2-10 LGAD 3	169.0 ± 3.2
W4 12-42 LGAD 1	154.9 ± 3.0

Sensor	Breakdown Voltage (V)
W4 12-42 LGAD 2	171.3 ± 3.3
W4 12-42 LGAD 3	171.4 ± 3.3
V1R5-32 LGAD 1	149.0 ± 2.8
V1R5-32 LGAD 2	157.6 ± 3.0
V1R5-32 LGAD 3	155.9 ± 2.9
V1R5-13 LGAD 1	167.2 ± 3.2
V1R5-13 LGAD 2	158.6 ± 3.0
V1R5-13 LGAD 3	159.5 ± 3.0
W1R2-27 LGAD 1	174.9 ± 3.2
W1R2-27 LGAD 2	163.5 ± 3.1
W1R2-27 LGAD 3	164.1 ± 3.1
W4 12-49 LGAD 1	202.9 ± 3.9
W4 12-49 LGAD 2	182.5 ± 3.5
W4 12-49 LGAD 3	182.5 ± 3.5
V1R5-33 LGAD 1	176.0 ± 3.3
V1R5-33 LGAD 2	158.7 ± 3.0
V1R5-33 LGAD 3	159.8 ± 3.0
V1R5-14 LGAD 1	257.5 ± 4.9
V1R5-14 LGAD 2	221.1 ± 4.2
V1R5-14 LGAD 3	220.4 ± 4.2
W1R2-20 LGAD 1	274.6 ± 5.2
W1R2-20 LGAD 2	240.1 ± 4.9
W1R2-20 LGAD 3	244.2 ± 4.9
W1R2-12 LGAD 1	188.4 ± 3.6
W1R2-12 LGAD 2	173.8 ± 3.5
W1R2-12 LGAD 3	173.6 ± 3.5
W4 12-27 LGAD 1	287.3 ± 5.5
W4 12-27 LGAD 2	236.0 ± 4.5

Sensor	Breakdown Voltage (V)
W4 12-27 LGAD 3	240.3 ± 4.7
V1R5-34 LGAD 1	206.0 ± 3.9
V1R5-34 LGAD 2	194.5 ± 3.7
V1R5-34 LGAD 3	192.1 ± 3.6